Talanta 312 (2027) 130316

Contents lists available at ScienceDirect

Talanta

journal homepage: www.elsevier.com/locate/talanta

Influence of graphene-based ink formulation on the performance of inkjet-printed electrochemical sensors for detecting water contaminants of emerging concern

Lucía Quintana [a], Sonia Melendi-Espina [b,c], Colin F. Dowding [b], Patricia Álvarez [a], Marcos Granda [a], Rosa Menéndez [a], Zoraida González [a,*]

[a] Instituto de Ciencia y Tecnología del Carbono, INCAR (CSIC), Francisco Pintado Fe 26, Oviedo, 33011, Spain
[b] School of Engineering, Mathematics and Physics, University of East Anglia, Norwich Research Park, Norwich, NR4 7TJ, UK
[c] Instituto de Carboquímica, ICB (CSIC), Miguel Luesma Castán 4, Zaragoza, 50018, Spain

ARTICLE INFO

Keywords:
Inkjet printing
Graphene-based ink
Ink formulation
Electrochemical sensing
Water emerging contaminants

ABSTRACT

Inkjet printing has emerged as a promising approach for the fabrication of low-cost and scalable electrochemical sensors, particularly when carbon-based nanomaterials are used. This study investigates the influence of graphene-based ink formulation on the performance of inkjet-printed sensors designed for the detection of acetaminophen, a pharmaceutical product identified as a water contaminant of emerging concern. Two ink formulations were prepared, each containing an aqueous graphene oxide suspension as the functional material, Triton X-100 as a surfactant, and carbon black as a conductive additive. However, they differed in their solvent systems, with the aim of optimising both, ink printability and the electrochemical response of the resulting sensors. The printed electrodes' morphology, pattern topography/uniformity, electrical conductivity, surface chemistry and electrochemical performance toward target analyte were characterized. Our findings reveal that ink composition significantly impacts film uniformity, electron transfer kinetics, and overall sensor performance. The formulation incorporating a mixed solvent system (water, glycerol, ethylene glycol) exhibited superior performance, achieving lower detection limits (LOD ~ 0.572 μM) and enhanced reproducibility and repeatability (% RSD ~ 5.3 and 5.7, respectively) for acetaminophen sensing. These results highlight that rational ink formulation is not merely an optimization parameter, but a decisive design factor that markedly influences the performance of printed electrochemical sensors, establishing it as a critical element for advancing reliable and high-impact environmental monitoring technologies.

1. Introduction

The growing presence of emerging contaminants in natural and wastewater systems has become a major environmental concern due to their persistence, widespread distribution, and potential adverse effects on both ecosystems and human health [1,2]. Among these contaminants, pharmaceuticals are frequently detected due to their high consumption and incomplete removal during conventional wastewater treatment, which allows them to enter aquatic environments at nano-to micromolar concentrations [3]. Paracetamol, a widely used analgesic and antipyretic commonly known as acetaminophen (N-acetyl-p-aminophenol - ACF), is one of the most commonly reported pharmaceutical pollutants. Its continuous discharge into the environment, together with its demonstrated toxicity to aquatic organisms, highlight the need for sensitive, selective, and cost-effective analytical strategies for detection in real samples [4].

Electrochemical sensors have emerged as attractive alternatives to traditional analytical techniques due to their operational simplicity, low cost, rapid response, and compatibility with miniaturised platforms [5,6]. The incorporation of carbon-based nanomaterials, including graphene, graphene oxide (GO), and thermally reduced graphene oxide (TRGO), is known to significantly enhance electrocatalytic activity, electron-transfer kinetics, and sensitivity [7,8]. However, the processing route used to integrate these materials onto conventional sensing substrates (such as glassy carbon electrodes, GCEs, or screen-printed electrodes, SPEs) plays a decisive role in determining their final

* Corresponding author.
E-mail address: zoraidag@incar.csic.es (Z. González).

https://doi.org/10.1016/j.talanta.2026.130316
Received 4 April 2026; Received in revised form 24 June 2026; Accepted 14 July 2026
Available online 14 July 2026

performance, particularly with respect to film uniformity, particle connectivity, and accessibility of electroactive sites to target analytes.

To overcome these limitations and advance the development of next-generation point-of-care electrochemical sensors, inkjet printing (IP) has emerged as a highly versatile and scalable fabrication technique. Its growing relevance stems from its ability to deposit functional materials in a contactless manner with precise spatial control, while requiring minimal amounts of ink [9,10]. To ensure stable droplet formation and pattern definition of the sensing platform, inks must meet specific physicochemical requirements, including viscosity, surface tension, density, and wettability. These properties are often summarized by the dimensionless printability parameter (Z), which typically ranges between 1 and 14. Ink formulation therefore becomes a critical design factor. Even small variations in the solids content, surfactant concentration, or solvent composition can markedly influence droplet dynamics, film morphology, and ultimately the electrochemical performance of the printed electrodes [11–13].

In addition to printability, several key factors must be considered when formulating an ink for a specific sensing application, including the physicochemical characteristics of the target analytes and the faradaic processes governing their detection mechanisms. In this context, the selection of an appropriate functional material is crucial for achieving sensitive, selective and robust electrochemical sensors. Among the various options, nanocarbons, particularly graphene and related materials, have emerged as promising candidates due to their exceptional properties [14–17].

Graphene oxide (GO) stands out as an excellent precursor for formulating specific inks for inkjet-printed electrochemical sensors. Its inherent aqueous dispersibility enables the preparation of stable colloids with low surfactant content at practical concentrations, while its abundant oxygen-containing functional groups provide tuneable rheology and surface tension compatible with reliable droplet formation. In parallel, the rich and versatile surface chemistry of GO facilitates robust film formation, controllable porosity, and straightforward functionalisation with recognition elements, thereby improving selectivity without compromising print fidelity [18–21]. Moreover, post-printing thermal, chemical or electrochemical reduction partially restores the Csp^2-hybridised network, yielding reduced graphene oxide (rGO) with significantly enhanced electrical conductivity and appropriate number of electroactive sites, both essential for efficient charge transfer and high signal-to-noise ratios [22–24]. Collectively, these properties make GO-based inks a versatile and scalable platform for producing sensitive, selective, and reproducible point-of-care sensing sensors by inkjet printing.

Despite this potential, the relationships between ink formulation, the resulting microstructure of the printed film, and its electrochemical behaviour remain insufficiently understood, although they are fundamental for the rational development of optimized sensing platforms.

In this work, we systematically investigate the influence of GO-based ink formulation on the physicochemical properties, morphology, and electrochemical performance of inkjet-printed sensing platforms (IPEs) designed for ACF detection. Two GO-based inks, differing primarily in their solvent systems (water vs. a water/glycerol/ethylene glycol mixture), were formulated and evaluated in terms of printability, film formation, microstructure, surface chemistry, and electron-transfer kinetics after thermal treatment. The findings highlight the decisive role of ink formulation in achieving uniform, conductive, and electrochemically active electrodes, with the mixed-solvent formulation showing superior electrochemical performance for ACF sensing.

2. Experimental

2.1. Synthesis of graphene oxide aqueous suspension

Graphene oxide (GO) aqueous suspension was synthesized using a modified Hummer's method, as described elsewhere [25]. Briefly, synthetic graphite powder (Sigma Aldrich, particle size <20 μm) was oxidised by reaction with a mixture of concentrated sulfuric acid (95-97%, Scharlab, Setmenant, Spain) and sodium nitrate (Scharlab, Setmenant, Spain) under continuous stirring. Potassium permanganate (Scharlab, Setmenant, Spain) was gradually added, and the reaction mixture was stirred for 3 h at 35°C. Subsequently, hydrogen peroxide (3% w/w, Scharlab, Setmenant, Spain) was slowly introduced to control the highly exothermic nature of the reaction, followed by an additional hour of stirring to ensure complete oxidation. The resulting suspension was centrifuged, and the supernatant discarded. To reach neutral pH, the product was repeatedly washed by centrifugation with deionised water and then filtered. The obtained graphite oxide was exfoliated by mild sonication for 8 h, yielding a yellow-brown graphene oxide suspension.

2.2. Formulation and characterization of graphene-oxide based inks

Starting from the previously synthesized GO aqueous suspension (4000 ppm), two distinct ink formulations (*Ink 1* and *Ink 2*) were prepared, differing mainly in their solvent systems. *Ink 1* used Milli-Q water as the sole solvent, whereas *Ink 2* employed a mixed solvent system consisting of 30 wt% glycerol and 20 wt% ethylene glycol in water. In both formulations, carbon black (CB; Cabot) was incorporated as a conductive additive at a GO:CB weight ratio of 35:1, and Triton® X-100 (TX-100; Thermo Fisher Scientific) was added as a surfactant at a GO: TX-100 ratio of 2:1 (wt.%). The selected formulations were not intended to exhaustively cover the full formulation space of graphene-based inks, but rather to compare two representative solvent-design strategies while keeping the active carbon-based components constant.

Once prepared, and after filtration through 1 μm glass fibre filters (Whatman), both inks were characterized in terms of viscosity, contact angle on Kapton® substrate (DuPont™), density, and surface tension. Viscosity was measured using a Brookfield viscosimeter equipped with a small sample adapter, operated at 200 rpm and room temperature. Contact angle measurements were performed using a Krüss goniometer (DSA25, Drop Shape Analyzer) equipped with a standard CF04 camera. A 5 μL droplet of each ink was deposited onto the substrate, and the angle was recorded once the droplet stabilized. Data were processed using the instrument's software. Each droplet was dispensed with a disposable 1 mL syringe with a 0.5 mm stainless-steel needle.

Inks density was determined using a pycnometer (Brand, Wertheim, Germany). Surface tension was measured by acquiring pendant-drop images with the Krüss DSA25/CF04 system and analysing them using Fiji (Image J) software through shape-fitting evaluation. All measurements were performed in triplicate.

Based on these parameters, the printability number (Z) was calculated according to the following equation:

$$Z = \sqrt{\rho\gamma D} \Big/ \eta$$

where η, γ, ρ and D represent ink viscosity (mPa s), surface tension (mN m^{-1}), density (g cm^{-3}), and nozzle inner diameter (μm), respectively. According to the literature, printable inks typically exhibit Z values in the range of 1-14 [26].

2.3. Inkjet-printing, post-processing and physicochemical characterisation of graphene-based sensing platforms

GO-based IPEs (IPE-1 and IPE-2) derived from inks under evaluation were fabricated using a commercial desktop printer (Epson XP-2200, injector diameter: 23 μm), with the standard print resolution mode (approximately 726 drops per inch, corresponding to an estimated drop spacing of 35 μm), and Kapton® (DuPont™) as flexible substrate. To ensure smooth printer operation, external ink tanks (CISS deposits, Luxury Plus, Bioprinter) were used, enabling easy filling with the different inks, as well as emptying and cleaning with Milli-Q to remove

any residual material. Prior to printing, *Inks 1* and *2* were homogenised using a Speed Mixer (Hauschild, model DAC 150.1 FVZ-K) for 10 min at 2000 rpm, and, as previously described, filtered through 1 μm glass fibre filters before being carefully introduced into the tanks to avoid bubbles formation. The IPEs were designed in a disk-shaped pattern (1 cm in diameter and 70-79 μm in thickness), using a conventional software, optimising the number of printed layers (up to 19), aiming to balance the homogeneity of the printed film and the ink/active material consumption. Considering an estimated GO loading of 1.05 μg/cm^2 per printed layer, the total amount of GO deposited was approximately 15.7 μg for the optimized 19-layer electrodes. After printing, IPE-1 and IPE-2 were subjected to a post-processing thermal treatment (400 °C, 1 h, N_2 flow: 200 mL min^{-1}), to enhance the electrical conductivity of the GO-based printed layers, since GO displays poor intrinsic conductivity. The treatment temperature was selected as a compromise between promoting partial GO reduction and preserving the integrity of the flexible Kapton substrate and the printed pattern, with the maximum temperature being limited by the thermal resistance of the substrate (Fig. S1, Supporting Information). The resulting electrodes were labelled as IPE-1_TT and IPE-2_TT, respectively.

The IPEs under evaluation were characterized using various techniques, to assess their physicochemical properties. As an initial approach, magnified images of both the as printed and thermally treated IPEs were obtained with an Olympus Corp. SZX10 stereo microscope, to evaluate the homogeneity and quality of the printed patterns. Their surface morphology was examined by means of SEM operating at 25 kW (FEI model Quanta FEG 650). In addition, the surface morphology of the IPEs_TT was also analysed using a confocal laser scanning microscope (OLS5000, Olympus Corp.), operated utilising both white light and laser interferometer illumination modes, one to provide qualitative overview of the coating uniformity, and the other to attempt quantitative assessment of the coating's surface topography. Morphological image processing in software (Matlab 2025b, Mathworks Inc.) employed consistent thresholding, smoothing, hole filling and boundary finding operations across all 5x magnification micrographs acquired by the confocal microscope (Fig. S2, supporting information). An automated feature counting algorithm was developed to provide a consistent treatment of substrate damage and differing illumination to yield a representative comparison between samples. Root mean square (RMS) surface roughness, *Rq*, and RMS waviness, *Wq*, values were calculated from levelled 20x magnification laser interferometer data acquired by the confocal microscope according to ISO 4287/2000 [27] in software (ImageJ). A sampling length of 200 μm was selected and a cutoff length of 40 μm applied through a Gaussian filter.

The surface chemistry of the electrodes was investigated by X-ray photoelectron spectroscopy (XPS) using a spectrometer equipped with a hemispherical electron analyzer and a MgKα ($h\nu$ = 1253.6 eV) X-ray source (Multilab 3000, VG-Microtech) by SPECS, Germany. The type of carbon bonding and oxygen functional groups were determined by curve fitting the C1s spectra using a Gaussian–Lorentzian peak shape after performing a Shirley background correction [28]. The related binding energy profiles were curve-fitted as follows: the main peak at 284.5 eV was assigned to Csp^2 and the other four peaks were attributed to Csp^3 (285.3 - 285.5eV), C–OH (286.4 - 286.6 eV), C═O (287.5-287.7 eV) and COOH functional groups (288.7 - 288.9 eV).

In addition, the sheet resistance of the inkjet-printed sensing platforms was evaluated using a Jandel RM3000+ test unit equipped with a Jandel cylindrical four-point probe head (Jandel Engineering, Leighton Buzzard, UK).

2.4. Electrochemical measurements

Electrochemical characterisation of the IPEs was carried out using a custom-made three-electrode cell (Fig. S3, Supporting Information), where the IPEs served as working electrodes (WE), an Ag/AgCl/3.5 M KCl electrode as the reference (RE), and a graphite rod as the counter electrode (CE). This configuration was selected to isolate the contribution of the printed WE and to specifically evaluate the effect of graphene-based ink formulation and printed pattern on the properties and electrochemical performance of the sensing platform. Therefore, the current IPE should be considered as an optimized sensing component rather than a fully integrated electrochemical device. To ensure reliable electrical contact between the IPEs and the Pt holder (and, subsequently with the potentiostat), a commercial silver ink (RS, Beuvais Cedex, France) was applied prior to the measurements. Cyclic voltammetry (CV) experiments were performed in the potential range of −0.2 – +0.8 V at various scan rates (clearly indicated). Differential pulse voltammetry (DPV) tests were conducted using optimized experimental parameters (t = 1 min 20 s, P_H = 100 mV, P_W = 25 mV, S_H = 5.0 mV, S_T = 200 mS). Electrochemical impedance spectroscopy (EIS) experiments were performed at frequencies from 100 KHz to 100 mHz using a potential of 0.25 V. The selected electrolyte consisted of 0.1 M KCl containing 5 mM $[Fe(CN)_6]^{3-/4-}$, as a redox probe to obtain preliminary information about the electron transfer resistance of the different sensing platforms. All experiments were conducted at room temperature using a VMP3 potentiostat-galvanostat (Bio-Logic, France), with a 0.1 M phosphate buffer (PBS) solution, at optimized pH and containing specified concentrations of the target analyte, as the electrolyte.

3. Results and discussion

3.1. Impact of graphene-based ink formulation on the physicochemical properties of the sensing platforms

To elucidate the impact of ink formulation on the properties of the printed sensing platforms, a comprehensive analysis of their key inkjet-relevant properties was performed (Table 1).

As expected, *Ink 1*, formulated with water as the sole solvent, exhibited low viscosity (1.85 mPa s) and high surface tension (32.20 mN/m), properties that favour stable droplet formation, as previously reported [29,30]. However, its slightly lower density (0.999 g/mL) may limit the amount of active material deposited per layer, potentially reducing the performance of the resulting film. In contrast, *Ink 2*, prepared using a mixture of water and organic solvents, showed higher viscosity (8.10 mPa s) and density (1.098 g/mL), enabling the fabrication of more robust and conductive sensing platforms. Although its lower surface tension (24.79 mN/m) could compromise pattern resolution, the printability parameter (Z = 3.09) falls within the optimal range reported in the literature [31], together with the higher solid content, may contribute to platforms of improved quality. Moreover, contact angle measurements on Kapton substrates (30.4 ± 0.9 and 27.1 ± 1.0 for *Inks 1 and 2*, respectively) suggest that *Ink2* exhibits slightly better wettability, promoting improved spreading and adhesion during printing. This behaviour may help compensate for its lower surface tension, thereby contributing to more uniform films. These findings are consistent with previous studies, highlighting the importance of simultaneously optimising viscosity and solid concentration to achieve improved performance in electroanalytical applications [32].

To further illustrate the influence of ink formulation on the resulting printed patterns, Fig. 1 shows optical images of the as printed (included for comparison) and those subjected to thermal treatment. These images reveal clear differences in pattern uniformity and edge definition, which

Table 1
Physical properties and printability parameter of the inks.

Ink	Viscosity/ŋ (mPa · s)	Contact angle ( )	Surface tension/γ (mN/m)	Density/ρ (g/mL)	Printability parameter (Z)
1	1.85	30.4° ± 0.9	32.20	0.999	14.71
2	8.10	27.1° ± 1.0	24.79	1.098	3.09

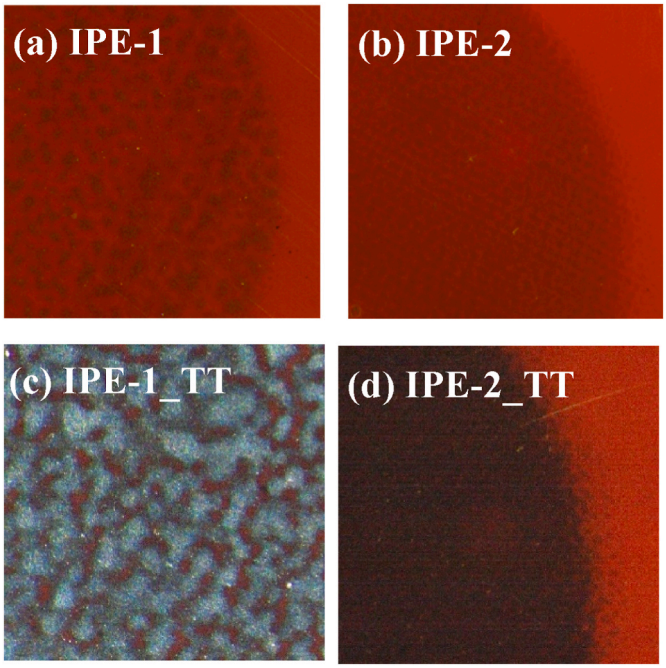

Fig. 1. Magnified images (x 20) of both the as-printed (a, b) and thermally treated (c, d) IPEs from the different Inks.

correlate with the key ink properties previously discussed. In particular, the films printed with *Ink 2* display a more continuous and homogeneous coverage, consistent with its higher viscosity and solid content, whereas *Ink 1* tends to produce less uniform layers. Notably, even after the thermal post-treatment, the sensing platforms printed with *Ink 2* maintained their better morphology, further supporting the suitability of this formulation.

Building on the above results, SEM images allow a deeper examination of the microstructure of the printed electrodes (Fig. S4). Consistently with previous optical observations, the electrode printed with *Ink 1* (IPE-1) exhibits a noticeably more heterogeneous morphology, with regions of discontinuous coverage, leaving the substrate partially exposed. In contrast, IPE-2 displays a more compact microstructure, characterized by a continuous distribution of graphene-based material and fewer visible defects. This improved morphology aligns with the enhanced wettability, higher viscosity, and greater solid content previously discussed for *Ink 2,* which contribute to a more controlled spreading of droplets when printing, facilitating the formation of homogeneous films [26].

The thermal post-processing further confirms these differences. While IPE-1_TT shows limited improvement after heating, maintaining regions with incomplete coverage, IPE-2_TT retains its uniform microstructure, suggesting stronger particle interaction and an appropriate consolidation process upon annealing [33].

Confocal microscopy images confirm these differences in the morphology of the printed patterns produced with the two ink formulations. In the micrographs shown in Fig. 2, mid-grey areas correspond to deposited ink, bright areas indicate the uncoated substrate, and dark features arise from substrate surface imperfections or optical refraction effects. The behaviour of the ink-surface wetting is altered by both the ink formulation and the effect of thermal treatment.

Electrodes printed with *Ink 1* (a, b, e and f in Fig. 2) exhibit less defined and more irregular spot geometries, suggesting less controlled droplet spreading and deposition during the printing process. In contrast, *Ink 2* (c, d, g and h) produces more uniform tracks with better-defined boundaries, indicating improved wetting behaviour and coalescence on the substrate.

After thermal treatment, both ink formulations exhibit a darker appearance, consistent with the thermal reduction of GO and the partial restoration of the conductive carbon network. However, differences in the morphology of the printed films remain visible. For *Ink 1*, annealing appears to promote the formation of larger, more continuous patches across the printed region, suggesting that the deposited material becomes distributed over broader areas. This is supported by the morphological analysis data provided in Table 2, which reports a 308% increase in deposited area (46.5 pixels for IPE-1 *vs* 143 pixels for IPE-

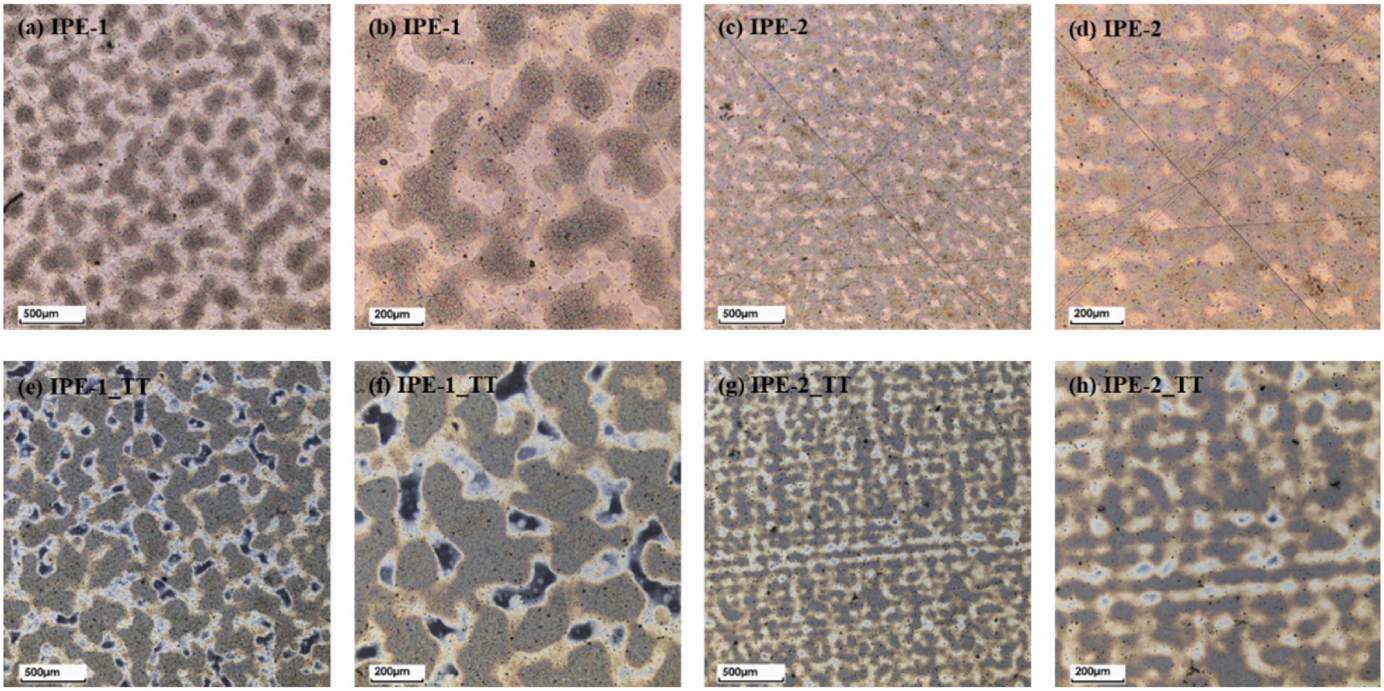

Fig. 2. IPE-1 at (a) 5x magnification and (b) 10× magnification; IPE-2 at (c) 5x magnification and (d) 10× magnification; IPE-1_TT at (e) 5x magnification and (f) 10× magnification; IPE-2_TT at (g) 5x magnification and (h) 10× magnification.

Table 2
Deposited ink spot statistics resulting from morphological analysis.

Ink	IPE-1	IPE-2	IPE-1_TT	IPE-2_TT
Spots per mm^2	75	101	49	159
Mean Spot Area (pixels)	46.5	25.9	143	7.6
RMS Surface Roughness, *Rq* (μm)	15.1	10.2	14.5	10.1
RMS Surface Waviness, *Wq* (μm)	6.0	3.1	15.1	10.6
$Wq/\sqrt{Area}$	0.35	0.24	0.51	1.54

Table 3
Sheet resistance of the inkjet-printed sensing platforms.

Sensing platform	Sheet resistance (kΩ/sq)
IPE-1	No measurable
IPE-2	No measurable
IPE-1_TT	4.57 ± 0.57
IPE-2_TT	3.76 ± 0.13

1_TT) and a halving of the recognised independent features per unit area.

In contrast, the films printed with *Ink 2* show a noticeable improvement in definition after the thermal processing, making the rows of the printhead spray pattern readily recognisable in Fig. 2 (g). This is accompanied by a 157% increase in deposited spot density (101 spots/mm^2 for IPE-2 *vs* 159 spots/mm^2 for IPE-2_TT) and a 3.4-fold reduction in the mean discrete spot area (Table 2). It indicates that, while thermal treatment modifies the morphology of both films, the underlying deposition characteristics associated with each ink formulation remain evident.

Roughness data, *Rq*, presented in Table 2 quantifies the topology of small surface asperities in the samples (Fig. S5). *Rq* values are subject to influence by non-ink features present upon the samples' substrates (e.g., scratches). It is assumed that all sample substrates exhibit similar non-ink features; hence, although the absolute values may be excessive when considering just the ink surface, it is instructive that the *Ink 1* samples exhibit significantly larger *Rq* values than the *Ink 2* samples.

Waviness (*Wq*) is used as an indicator of the vertical height variation of deposited droplets, as it is less sensitive to underlying substrate features. *Ink 1* shows higher *Wq* than *Ink 2* both before and after thermal treatment, suggesting that its greater height is partly inherited from the initial film morphology and amplified during heating. Initially, *Ink 2* droplets are approximately half the height of those formed from *Ink 1*. After thermal treatment, this difference decreases, with IPE-2_TT reaching around 70% of the height of IPE-1_TT.

Thermal processing leads to the evolution of gaseous species (e.g., CO_2, CO), whose out-of-plane escape induces vacancy defects and structural disorder, resulting in roughened and crumpled morphologies with increased surface waviness [34,35].

To further assess spot morphology, a height-to-width parameter was estimated by normalising *Wq* with the square root of the mean droplet area. The area values, initially obtained in pixels from image analysis, were converted into microns using the calibration factor shown in Fig. S2 (160 pixels = 100 μm). This normalization yields a dimensionless parameter that provides an indication of the droplet aspect ratio (Table 2). Prior to thermal treatment, *Ink 2* displays a lower height-to-width ratio than *Ink 1*, indicating a more laterally spread droplet. This observation agrees with the lower contact angles reported for *Ink 2* (Table 1). Annealing significantly alters droplet morphology for both inks. *Ink 1* shows a 143.5% increase in height-to-width ratio (0.35 to 0.51, Table 2), suggesting moderate contraction. However, *Ink 2* exhibits a substantially larger increase of approx. 630% (from 0.24 for IPE-2 to 1.54 for IPE-2_TT), indicating a pronounced reduction in lateral spread and a transition towards a more compact, dome-like structure. This suggests that *Ink 2* droplets undergo significant recession in contact area during thermal treatment.

The formation of a more dome-like morphology following thermal treatment is consistent with densification and contraction of the reduced GO network, which likely enhances electrical performance by improving inter-flake contact and increasing conductive pathways, resulting in reduced resistance and improved electrode behaviour [36–39]. In fact, this is reflected in the sheet resistance measurements, where the electrode IPE-2_TT shows a significantly lower sheet resistance (3.76 ± 0.13 kΩ/sq) than IPE-1_TT (4.57 ± 0.57 kΩ/sq) (Table 3). Dome-like morphologies are sometimes associated with poor film uniformity; however, in this case, the enhanced electrical performance suggests that improved inter-flake connectivity outweighs any loss in lateral coverage, consistent with previous studies [40].

The lower sheet resistance observed for IPE-2_TT compared to IPE-1_TT suggests that ink formulation also plays a critical role in determining the final electrical properties. These results also confirm the key impact of post-printing treatments and ink optimization for achieving suitable sensing platforms.

To complement the morphological and electrical characterisation, the chemical composition of the IPEs was investigated by XPS (Table 4). This analysis provides insight into the surface chemistry, which also plays a determining role in the subsequent sensing performance.

According to the results summarized in Table 4, directly printed electrodes exhibit a higher oxygen content, which is consistent with the presence of oxygenated functional groups from GO and residual additives. After the post-processing step, the oxygen content markedly decreased to 14.7 at. % for IPE-1_TT and 11.4 at. % for IPE-2_TT, being this value accompanied by an increase in carbon content. This removal of oxygen functionalities is consistent with a partial restoration of the graphitic network, as confirmed by the curve-fitting of the C1s spectra obtained from the different sensing platforms (Fig. S6 and Table S1, Supporting Information), also correlating with the observed decrease in sheet resistivity (Table 3). After the thermal treatment, both IPE-1 and IPE-2 exhibit a substantial increase in Csp^2 content accompanied by a marked decreased in C–O functionalities (from approx. 38-39% to 9-10%). These trends are consistent with established C1s fitting models for graphene-based materials and the widely known thermal deoxygenation of GO to thermally reduced graphene oxide (TRGO), wherein hydroxyl/epoxy groups are removed at lower temperatures [41].

In addition, a small amount of N was detected in all samples even though this signal originates from the Kapton substrate and does not reflect changes in the printed layer. The morphological improvements observed in SEM and confocal images, together with the chemical changes revealed by XPS, confirm that thermal treatment enhances particle connectivity and removes insulating species, thereby promoting efficient electron transport. These combined effects are critical for optimising the performance of inkjet-printed sensing platforms.

3.2. *Preliminary screening of the electrochemical performance of IPEs for ACF sensing*

In agreement with the previous observations, the thermally post-processed printed electrodes (IPE-1_TT and IPE-2_TT) were selected as sensing platforms to evaluate their performance for ACF sensing [42]. As an initial approach, CV and DPV experiments (Fig. 3 (a) and 3 (b)) were carried out in a customised three-electrode cell (Fig. S3, Supporting Information), using these sensing platforms as WEs (see Experimental Section for details).

The CVs recorded on both electrodes exhibit well-developed anodic

Table 4
Surface chemical composition of the inkjet-printed sensing platforms (at. %).

Sensing platform	C	O	N
IPE-1	75.3	24.1	0.6
IPE-2	68.8	29.8	1.4
IPE-1_TT	82.2	14.7	3.1
IPE-2_TT	86.6	11.4	2.0

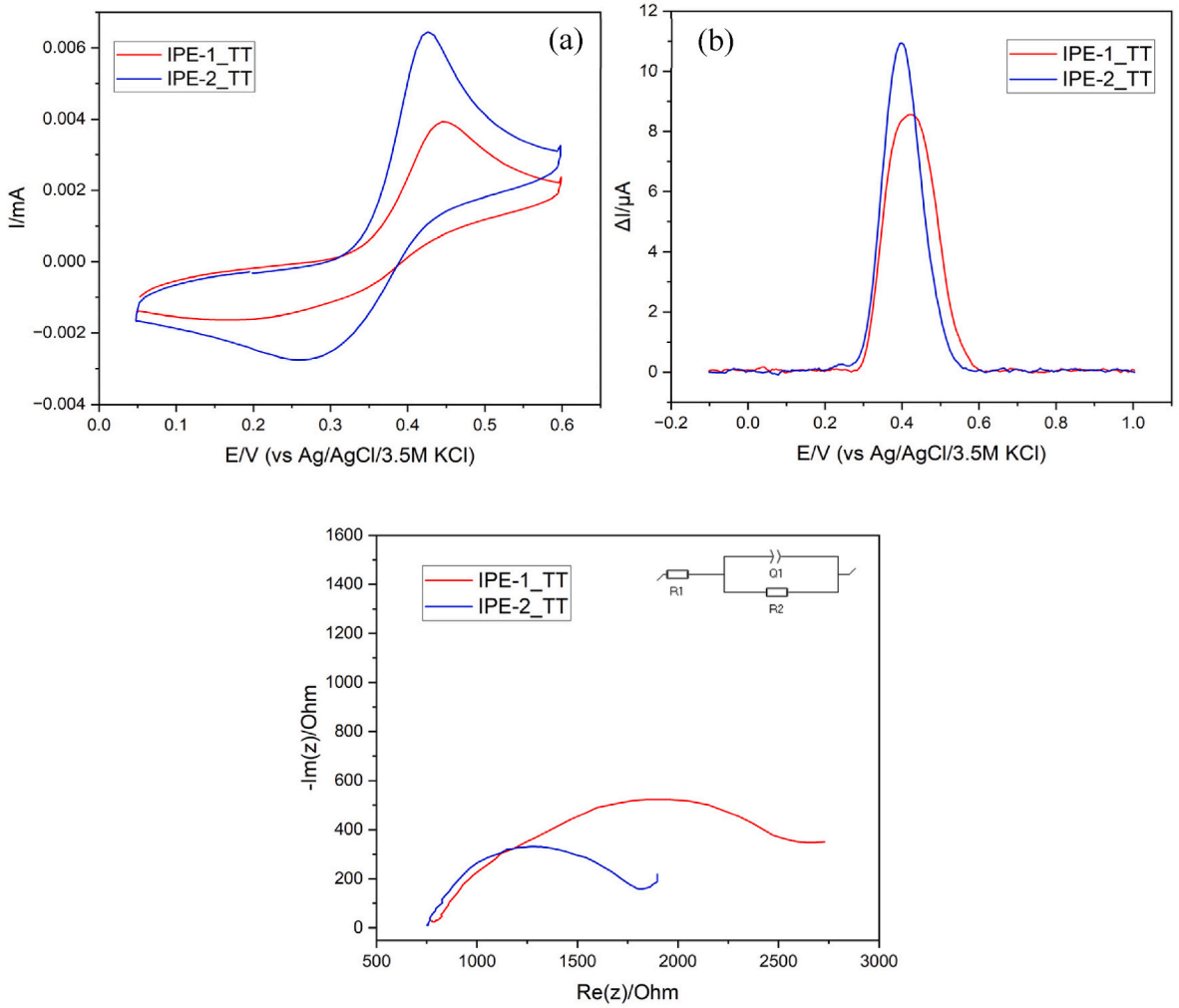

Fig. 3. CVs recorded at 5 mV/s (a) and baseline-corrected DPVs obtained (b), on the IPEs under evaluation, in 0.1 M PBS (pH = 7.0) containing 100 μM of ACF. Nyquist plots (c) recorded on the same sensing platforms in 0.1 M KCl containing 5 mM $[Fe(CN)_6]^{3-/4-}$ at a formal potential of 0.25 V and a frequency range of 100 KHz – 100 mHz. The inset shows the equivalent circuit selected to fit the impedance data.

and cathodic peaks corresponding to the reversible faradaic processes involving ACF and its main metabolite, N-acetyl-p-benzoquinone-imine. IPE-2_TT exhibits higher oxidation and reduction peak currents, lower peak-to-peak separation, and improved anodic and cathodic overpotentials, indicating a better electrochemical activity towards ACF sensing [43]. Furthermore, DPV measurements confirm this trend, with IPE-2_TT showing a sharper and more intense oxidation peak, which translates into greater sensitivity for ACF detection [44]. These results are further supported by the Nyquist plots (Fig. 3 (c)), where IPE-2_TT exhibits a significantly smaller diameter of the semicircle developed at high frequencies, which is in agreement with a lower charge-transfer resistance ($Rct = 1.1 \pm 8.4 \times 10^{-3}$ KΩ vs. $2.2 \pm 17.4 \times 10^{-3}$ KΩ for IPE-1_TT) and improved electron transfer kinetics at the electrode/electrolyte interface [45]. This result is also consistent with the enhanced conductivity of IPE-2_TT, which facilitates faster electron kinetics (apparent $K^0 = 6.2 \times 10^{-5}$ cm/s vs. 3.1×10^{-5} cm/s for IPE-1_TT [46]) and contributes to its superior electrochemical response. To evaluate whether the enhanced electrochemical response of IPE-2_TT was associated with an increased electroactive surface area, the double-layer capacitance (C_{dl}) was estimated from CVs recorded at different scan rates in a non-faradaic potential window (Fig. S7, Supporting Information). The calculated C_{dl} values were very similar for IPE-1_TT and IPE-2_TT, indicating comparable electrochemically accessible surface areas. This similarity is consistent with the fact that both electrodes were produced using the same printing design, exhibited the same nominal geometrical area, and were subjected to the same thermal treatment. Therefore, the improved electrochemical performance of IPE-2_TT does not seem to arise from a larger electroactive area, but rather from enhanced electrical connectivity within the printed film and more efficient charge transfer at the electrode/electrolyte interface, as evidenced by its lower *Rct* and higher apparent K^0. Based on these results, IPE-2_TT was selected for subsequent investigations.

3.3. Performance of the IPE-2_TT-based sensor

After identifying IPE-2_TT as the most promising sensing platform, the next step focused on optimising key experimental parameters to maximise its performance for ACF detection. Among these, electrolyte pH value and CV scan rate were systematically investigated, as both strongly influence the redox behaviour, peak definition, and electron transfer kinetics of the analyte. This optimization aimed to establish the conditions that provide the highest sensitivity and reproducibility, ensuring reliable operation of the inkjet-printed sensor in practical applications.

3.3.1. Optimization of the operational pH value

The influence of the pH of the PBS solution on the electrochemical response of IPE-2_TT towards ACF detection was systematically

evaluated in the range of 5.8 – 8.0 by CV measurements (Fig. 4 (a)). Additionally, the effect of pH on both the oxidation peak potential and the corresponding anodic current, was analysed (Fig. 4 (b)).

The results indicate that the electrochemical oxidation of ACF is significantly affected by the pH of the supporting electrolyte, as expected for faradaic processes involving proton-coupled electron transfer [47]. At lower pH values, the higher availability of protons stabilizes the oxidised species, shifting the oxidation potential to more positive values. Conversely, increasing the pH facilitates the oxidation process, as reflected by the negative shift in potential. To balance overpotential and anodic current for ACF oxidation on the evaluated IPE (0.04 mA, 0.42 V), a pH of 7.4 (a near-neutral value, representative of many natural and treated water matrices) was selected for subsequent studies.

3.3.2. *Influence of scan rate – mechanism controlling the kinetics of ACF detection*

The influence of scan rate on the electrochemical oxidation of ACF was further evaluated to elucidate the predominant kinetic control mechanism. As shown in Fig. 5 (a), the anodic peak current increases progressively with scan rate, accompanied by a slight positive shift in peak potential at higher rates. The linear relationship between peak current and the square root of the scan rate (Fig. 5 (b)), with $R^2 = 0.998$, indicates that the process on IPE-2_TT is, primarily diffusion-controlled [48].

Furthermore, the log-log plot of peak current vs. scan rate (Fig. 5 (c)) yields a slope of 0.51, close to the theoretical value of 0.5 expected for diffusion-controlled processes. Minor deviations at low scan rates suggest a slight contribution from adsorption phenomena, possible due to interactions between ACF and the graphene-based electrode surface (partial surface confinement of analyte molecules). In addition, the quasi-linear dependence of peak current on scan rate (Fig. 5 (d)) is in agreement with previous assumption, even though the anodic process on the proposed sensor is governed mainly by diffusion.

3.3.3. *Calibration curves, limit of detection, linear range and sensitivity of the IPE-2_TT sensor*

To evaluate the analytical performance of the IPE-2_TT sensor for ACF detection, DPV measurements were carried out, as this electrochemical technique is appropriate for measuring faradaic currents arising from redox processes [49,50].

Fig. 6 displays the baseline-corrected DPVs for increasing ACF concentrations, revealing a well-defined oxidation peak at 0.34V. The anodic peak current increases progressively with analyte concentration, confirming the sensor's ability to transduce concentration changes into reproducible faradaic signal. This behaviour reflects the efficient electron-transfer kinetics and the improved film homogeneity previously discussed for this sensing platform. The inset in Fig. 6 shows the corresponding calibration plot, resulting from experiments performed in triplicate for each ACF concentration, and the corresponding error bars. According to the results, a high linear response was obtained, with a correlation coefficient of $R^2 = 0.998$, thus corroborating the good linearity of the sensor and supporting the suitability of the optimized operational parameters. Based on the linear fit, the linear working range spans approximately 1- 30 μM, covering the relevant concentrations for practical monitoring scenarios in which ACF typically appears at low to mid-micromolar levels [51]. The sensitivity obtained from the slope of the calibration plot (0.432 μA/μM), which corresponds to an area-normalized sensitivity of 0.550 μA/μM·cm^2, reflects the analytical sensitivity of the sensor towards ACF and is associated with both the intrinsic electrocatalytic activity of the printed electrode surface and the effective accessibility of electroactive sites after thermal treatment. The estimated limit of detection (LOD = 0.572 μM) further highlights the potential sensor's capability for trace-level detection. It has been calculated using the conventional criterion $LOD = 3\sigma/m$, where σ is the standard deviation of 9 independent measurements of the blank signal and m is the slope of the calibration curve. LOD value is consistent with sensors designed and developed via inkjet printing of graphene-based materials. Post-printing thermal annealing promotes the formation of a conductive, low-defect network, which enhances electrochemical activity for the intended application. Notably, the obtained LOD positions the proposed sensor competitively when compared to other carbon-based disposable sensors reported in the literature (Table 5), despite the simplicity and low-cost nature of the fabrication route [59, 60].

3.3.4. *Interferences studies, reproducibility, and repeatability of the IPE-2_TT sensor for ACF detection*

Preliminary studies to evaluate the selectivity of IPE-2_TT towards ACF detection were carried out using diclofenac (DCF) and caffeine (CAF) as model interfering species. The selection of DCF is justified by its structural and electrochemical similarity with ACF, as they both are aromatic non-steroidal anti-inflammatory drugs containing redox active functional groups. In contrast, CAF was included as a structurally dissimilar yet electroactive compound of practical relevance, given its presence in pharmaceutical formulations combined with ACF. Furthermore, both DCF and CAF are classified as water contaminants of emerging concern [61,62].

As shown in Fig. S8, three well-defined oxidation peaks are developed (at + 0.37, +0.56 and + 0.95 V for ACF, DCF, and CAF, respectively) in the corresponding DPV. The observed peak separation and the absence of significant distortion in the ACF anodic peak (despite the higher concentration of the interfering species) suggests that, under the tested conditions, IPE-2_TT can differentiate the oxidation signals of ACF, DCF and CAF. However, this experiment should be regarded as a

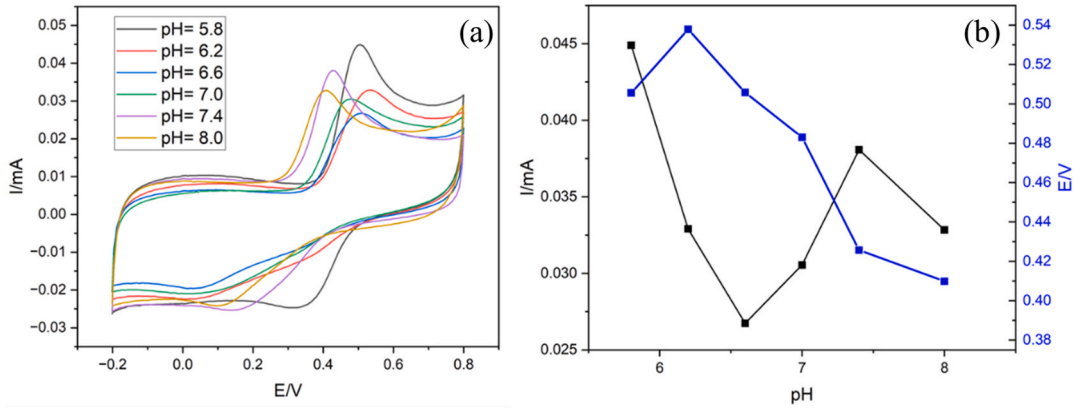

Fig. 4. CVs recorded on the IPE-2_TT electrode (scan rate = 100 mV/s) at increasing pH values in a 0.1 M PBS solution containing 100 μM of ACF (a). Effect of the pH on the anodic current and potential values corresponding to the ACF oxidation on this electrode (b).

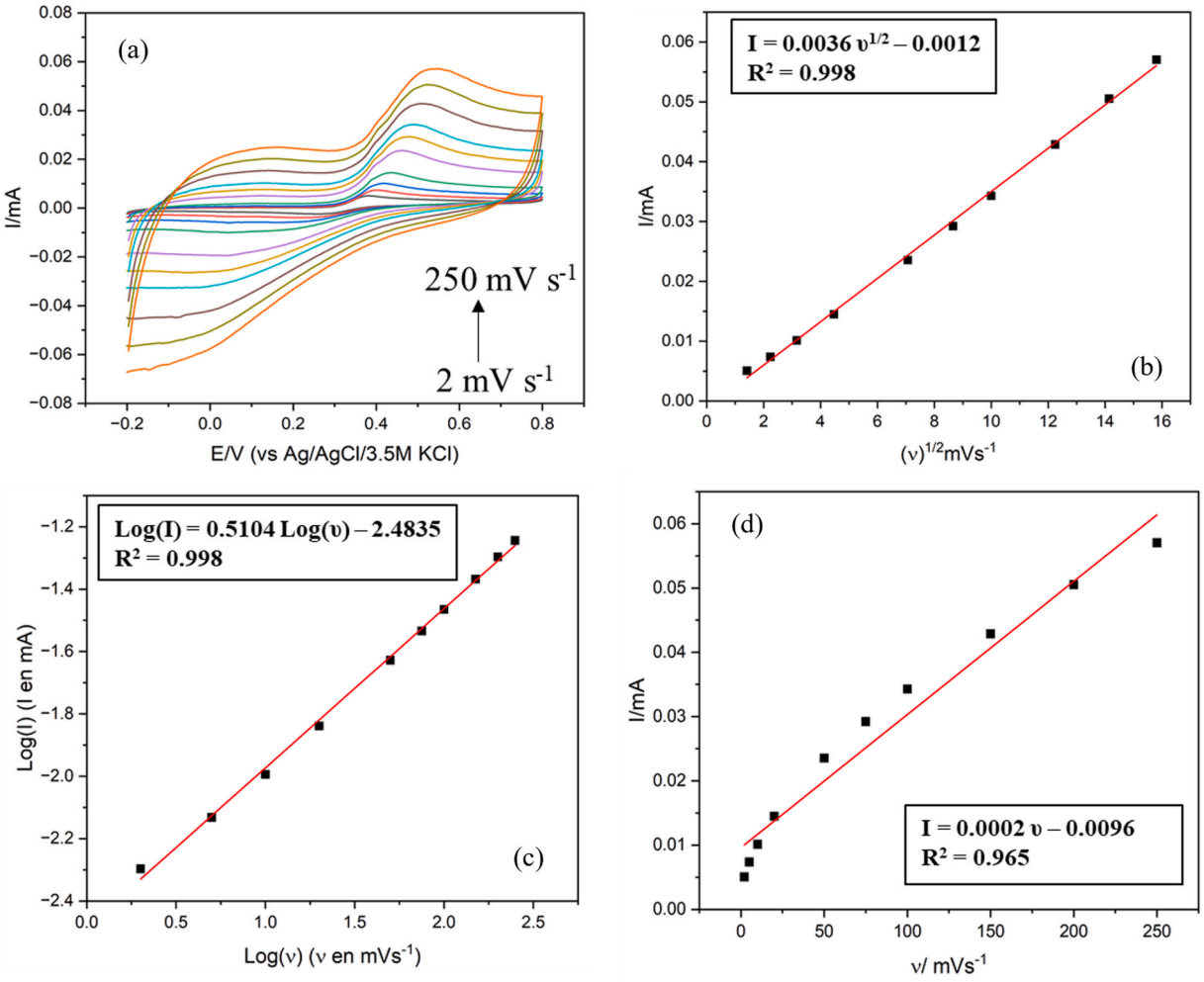

Fig. 5. CVs recorded on IPE2_TT at increasing scan rates in a 0.1 M PBS solution (pH = 7.4) containing 100 μM ACF (a). Linear correlation between the oxidation peak current and the square root of the scan rate (b). Logarithmic dependence of the anodic peak current on the scan rate (c). Correlation between the oxidation peak current and the scan rate (d).

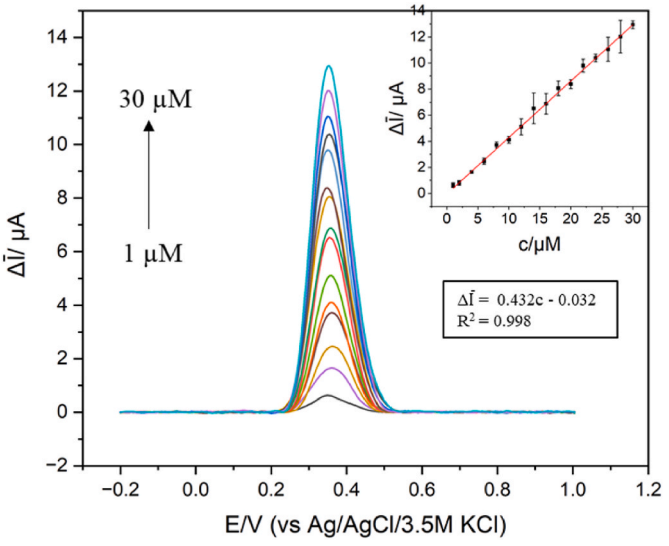

Fig. 6. Baseline corrected DPVs recorded on the IPE-2_TT electrode at increasing concentrations of ACF in 0.1 M PBS (pH = 7.4) (a). Inset: corresponding calibration curve with error bars, based on triplicate measurements.

Table 5
Sensor's performance for ACF sensing.

Sensor	LR (μM)	LOD (μM)	Sensitivity (μA/μM)	Reproducibility RSD (%)
Au/PANI-MWCNT/ biosensor [52]	5-6.3 × 10^2	2.9	---	0.62
PtNP/rGO-GCE [53]	5-100	3.0	0.06184 μA/μM	2.62
3D-printed CB-PLA [54]	---	0.15	0.714 μA/μM	---
NiCoFe LDH@g-CN [55]	0.166-1225.5	0.06	2.4338 μA/μM·cm^2	2.5
Fe-MOF/GR nanocomposite [56]	0.05-1105.6	0.01	6.7 μA/μM·cm^2	2.02
CeO_2/N-rGO-GCE [57]	1-200	0.79	0.1318 μA/μM	---
Graphene/ZrO_2/SPE [58]	10-100	0.0755	0.1171 μA/μM	<5
IPE-2_TT (This work)	1-30	1.104	0.548 μA/μM·cm^2	5.3

preliminary indication of discrimination capability rather than a comprehensive selectivity study. Additional experiments involving other coexisting contaminants will be addressed in future studies to establish the suitability of the sensor for complex environmental

matrices.

In addition, the reliability of this sensor was also assessed by means of reproducibility and repeatability tests (Figure S8 (b) and (c)). The reproducibility measurements, carried out using five different IPE-2_TT electrodes under identical conditions (100 μM ACF in 0.1 M PBS, pH = 7.4), display consistent DPVs peak potentials (~+ 0.34 V) and only minor variations in anodic peak current values (% RSD = 5.3 for current), confirming the robustness of the inkjet printing process and the uniformity of the sensing platform. Likewise, repeatability was assessed by performing five consecutive measurements with the same sensor under the same conditions. The resulting DPVs show negligible shifts in peak potential and minimal changes in peak current (% RSD = 5.7%), indicating suitable short-term stability. Together with previously shown selectivity results, these findings highlight the potential of IPE-2_TT for practical applications, where accurate detection of ACF in complex matrices requires not only discrimination from interfering species but also reliable and reproducible performance.

4. Conclusions

In this work, the influence of graphene-based ink formulation on the properties and electrochemical performance of inkjet-printed electrodes for acetaminophen detection was systematically evaluated. The results demonstrate that the solvent system plays a key role in governing the physicochemical behaviour of the inks, directly shaping film morphology, microstructure, surface chemistry and electrical conductivity of the resulting printed platforms. Compared with the water-based formulation, the mixed-solvent ink (water/glycerol/ethylene glycol) enabled the deposition of more homogeneous and continuous films, with reduced roughness and waviness, improved droplet definition, and a more compact microstructure after thermal treatment. These morphological advantages translated into enhanced electrical conductivity and a higher degree of graphitisation, as confirmed by XPS analysis. Overall, the findings highlight solvent engineering as a key strategy for tailoring the properties and performance of graphene-based inks, providing qualitative formulation guidelines that can support their rational design for specific sensing applications.

Electrochemical characterisation further revealed that the IPE-2_TT electrode exhibited superior electron-transfer kinetics, lower charge-transfer resistance, and more defined faradaic features towards acetaminophen oxidation than IPE-1_TT. As a consequence, the IPE-2_TT-based sensor showed improved analytical performance, including a well-defined linear range (1–28 μM), suitable sensitivity, a competitive limit of detection (0.572 μM), and excellent reproducibility and repeatability (RSD ≈ 5%). Moreover, a preliminary interference study using DCF as a structurally related electroactive compound suggests that this sensor can discriminate ACF under the tested conditions, supporting its potential for further evaluation in more complex water samples.

Overall, the results highlight that ink formulation is a fundamental design variable that governs the structure–property–performance relationships of inkjet-printed graphene-based sensors. Rational control over ink composition not only determines printability and film formation, but also dictates the electrochemical responsiveness of the final device. These findings provide a clear framework for the formulation of advanced graphene-based inks and offer valuable guidelines for the scalable fabrication of high-performance printed electrochemical sensors aimed at environmental monitoring applications.

CRediT authorship contribution statement

Lucía Quintana: Data curation, Investigation, Methodology, Writing – original draft. **Sonia Melendi-Espina:** Investigation, Writing – review & editing. **Colin F. Dowding:** Investigation, Writing – review & editing. **Patricia Álvarez:** Conceptualization, Funding acquisition, Supervision. **Marcos Granda:** Conceptualization, Funding acquisition, Supervision. **Rosa Menéndez:** Conceptualization, Funding acquisition, Project administration, Supervision, Writing – review & editing. **Zoraida González:** Conceptualization, Funding acquisition, Project administration, Supervision, Writing – review & editing.

Declaration of competing interest

The authors declare that they have no known competing financial interests or personal relationships that could have appeared to influence the work reported in this paper.

Acknowledgements

These results are part of the project PID2022-139478OB-100 funded by MICIU/AEI/10.13039/501100011033 and by FEDER, UE. L. Quintana also acknowledges her predoctoral contract (PREP2022-000270) associated with this project. The authors further acknowledge financial support from SEKUENS (Principality of Asturias Government) and EU-FEDER (IDE/2024/000737).

Appendix A. Supplementary data

Supplementary data to this article can be found online at https://doi.org/10.1016/j.talanta.2026.130316.

Data availability

Data will be made available on request.

References

[1] N. Morin-Crini, E. Lichtfouse, G. Liu, V. Balaram, A.R. Lado Ribeiro, et al., Worldwide cases of water pollution by emerging contaminants: a review, Environ. Chem. Lett. 20 (2022) 2311–2338, https://doi.org/10.1007/s10311-022-01447-4.
[2] M. Puri, K. Gandhi, M. Suresh Kumar, Emerging environmental contaminants: a global perspective on policies and regulations, J. Environ. Manag. 332 (2023) 117344, https://doi.org/10.1016/j.jenvman.2023.117344.
[3] J. Obinna Osuoha, B. Onyinyechi Anyanwu, C. Ejileugha, Pharmaceuticals and personal care products as emerging contaminants: need for combined treatment strategy, J. Hazard. Mater. Adv. 9 (2023) 100206, https://doi.org/10.1016/j.hazadv.2022.100206.
[4] N. Agarwal, Paracetamol – a contaminant of high concern: existence in environment and adverse effects, Pharmaceut. Drug. Regul. Aff. 4 (1) (2021) 000128, https://doi.org/10.23880/pdraj-16000128.
[5] E. Bakker, Y. Quin, Electrochemical sensors, Anal. Chem. 78 (12) (2006) 3965–3984, https://doi.org/10.1021/ac060637m.
[6] G. Hanrahan, D.G. Patil, J. Wang, Electrochemical sensors for environmental monitoring: design, development and applications, J. Environ. Monit. 6 (2004) 657–664, https://doi.org/10.1039/B403975K.
[7] F. Xie, M. Yang, M. Jiang, X.J. Huang, W.Q. Liu, P.H. Xie, Carbon-based nanomaterials – a promising electrochemical sensor toward persistent toxic substance, Trends Anal. Chem. 119 (2019) 115624, https://doi.org/10.1016/j.trac.2019.115624.
[8] L. Fritea, F. Banica, T.O. Costea, L. Moldovan, L. Dobjanschi, M. Muresan, S. Cavalu, Metal nanoparticles and carbon-based nanomaterials for improved performances of electrochemical (bio)Sensors with biomedical applications, Materials 14 (21) (2021) 6319, https://doi.org/10.3390/ma14216319.
[9] F. Zhang, M. Wei, V.V. Viswanathan, B. Swart, Y. Shao, G. Wu, C. Zhou, 3D printing technologies for electrochemical energy storage, Nano Energy 40 (2017) 418–431, https://doi.org/10.1016/j.nanoen.2017.08.037.
[10] A. Moya, G. Gabriel, R. Villa, F.J. del Campo, Inkjet-printed electrochemical sensors, Curr. Opin. Electrochem. 3 (1) (2017) 29–39, https://doi.org/10.1016/j.coelec.2017.05.003.
[11] K. Yamada, T.G. Henares, K. Suzuki, D. Citterio, Paper-based inkjet-printed microfluidic analytical devices, Angew. Chem. Int. Ed. 54 (2015) 5294–5310, https://doi.org/10.1002/anie.201411508.
[12] L. Nayak, S. Mohanty, S.K. Nayak, A. Ramadoss, A review on inkjet printing of nanoparticle inks for flexible electronics, J. Mater. Chem. C 7 (2019) 8771–8795, https://doi.org/10.1039/C9TC01630A.
[13] S. Magdassi, The Chemistry of Inkjet Inks, World Scientific Publishing Co. Pte. Ltd, 2010.
[14] T.H. Da Costa, E. Song, R.P. Tortorich, J.W. Choi, A paper-based electrochemical sensor using inkjet-printed carbon nanotube electrodes, ECS J. Solid State Sci. Technol. 4 (2015) S3044–S3047, https://doi.org/10.1149/2.0121510jss.
[15] H. Shamkhalichenar, J.W. Choi, An inkjet-printed non-enzymatic hydrogen peroxide sensor on paper, J. Electrochem. Soc. 164 (2017) B3101–B3106, https://doi.org/10.1149/2.0161705jes.

[16] M.A. Nalepa, D. Panáček, I. Dědek, P. Jakubec, V. Kupka, V. Hrubý, M. Petr, M. Otyepa, Graphene derivative-based ink advances inkjet printing technology for fabrication of electrochemical sensors and biosensors, Biosens. Bioelectron. 256 (2024) 116277, https://doi.org/10.1016/j.bios.2024.116277.
[17] M., T. Kant, , T., K. Shrivas, A. Kumar, K. Dewangan, Graphene-silver nano-ink for inkjet printing of paper electrode for electrochemical sensing of 4-nitrophenol, Mater. Chem. Phys. 304 (2023) 128161, https://doi.org/10.1016/j.matchemphys.2023.128161.
[18] P.P. Brisebois, M. Siaj, Harvesting graphene oxide– years 1859 to 2019: a review of its structure, synthesis, properties and exfoliation, J. Mater. Chem. C 8 (2020) 1517–1547, https://doi.org/10.1039/C9TC03251G.
[19] M.G. Gonçalves, V.O. Costa, A.H.G. Martínez, B.M. Règnier, G.C.B. Gomes, A.J. G. Zarbin, E.S. Orth, Functionalization of graphene oxide via epoxide groups: a comprehensive review of synthetic routes and challenges, Front. Carbon 3 (2024) 1393077, https://doi.org/10.3389/frcrb.2024.1393077.
[20] I. Ali, P.V. Oskin, T.P. Dyachkova, G. Imanova, A.A. Kovaleva, E.D. Dmitrieva, S. V. Alferov, T.A. Kurniawan, M. Messali, Advances in one-step functionalization of graphene oxide during electrochemical graphite exfoliation, J. Mater. Sci. 60 (2025) 13156–13190, https://doi.org/10.1007/s10853-11177-x.
[21] W. Yu, L. Sisi, Y. Haiyan, L. Jie, Progress in the functional modification of graphene/graphene oxide: a review, RSC Adv. 10 (2020) 15328–15345, https://doi.org/10.1039/D0RA01068E.
[22] D. Minta, Z. González, S. Melendi-Espina, G. Gryglewicz, Easy-to-prepare graphene-based inkjet-printed electrodes for diclofenac electrochemical sensing, Prog. Org. Coating 185 (2023) 107942, https://doi.org/10.1016/j.porgcoat.2023.107942.
[23] L. Huang, Y. Huang, J. Liang, X. Wan, Y. Chen, Graphene-based conducting inks for direct inkjet printing of flexible conductive patterns and their applications in electric circuits and chemical sensors, Nano Res. 4 (7) (2011) 675–684, https://doi.org/10.1007/s12274-011-0123-z.
[24] J. Kudr, L. Zhao, E.P. Nguyen, H. Arola, T.K. Nevanen, V. Adam, O. Zitka, A. Merkoçi, Inkjet-printed electrochemically reduced graphene oxide microelectrode as a platform for HT-2 mycotoxin immunoenzymatic biosensing, Biosens. Bioelectron. 156 (2020) 112109, https://doi.org/10.1016/j.bios.2020.112109.
[25] W.S. Hummers Jr., R.E. Offeman, Preparation of graphitic oxide, J. Am. Chem. Soc. 80 (6) (1958) 1339, https://doi.org/10.1021/ja01539a017.
[26] F. Torrisi, T. Hasan, W. Wu, Z. Sun, A. Lombardo, T.S. Kulmala, G.W. Hsieh, S. Jung, F. Bonaccorso, P.J. Paul, D. Chu, A.C. Ferrari, Inkjet printed graphene electronics, ACS Nano 6 (4) (2012) 2992–3006, https://doi.org/10.1021/nn2044609.
[27] G. Chinga, P.O. Johnssen, R. Dougherty, E. Lunden-Berli, J. Walter, Quantification of the 3-D microstructure of SC surfaces, J. Microsc. 227 (3) (2007) 254–265, https://doi.org/10.1111/j.1365-2818.2007.01809.x.
[28] second ed., in: M.P. Seah, D. Briggs (Eds.), Practical Surface Analysis: Auger and X-ray Photoelectron Spectroscopy, vol. 1, John Wiley & Sons, New York, NY, USA, 1990, p. 657.
[29] B. Derby, Inkjet printing of functional and structural materials: fluid property requirements, feature stability, and resolution, Annu. Rev. Mater. Res. 40 (2010) 395–414, https://doi.org/10.1146/annurev-matsci-070909-104502.
[30] P. Calvert, Inkjet printing for materials and devices, Chem. Mater. 13 (10) (2001) 3299–3305, https://doi.org/10.1021/cm0101632.
[31] D. Jang, D. Kim, J. Moon, Influence of fluid physical properties on ink-jet printability, Langmuir 25 (5) (2009) 2629–2635, https://doi.org/10.1021/la900059m.
[32] E.B. Secor, P.L. Prabhumirashi, K. Puntambekar, M.L. Geier, M.C. Hersam, Inkjet printing of high conductivity, flexible graphene patterns, J. Phys. Chem. Lett. 4 (8) (2013) 1347–1351, https://doi.org/10.1021/jz400644c.
[33] Q. He, S.R. Das, N. Garland, D. Jing, J.A. Hondred, A.A. Cargill, S. Ding, C. Karunakaran, J.C. Claussen, Enabling inkjet-printed graphene for ion selective electrodes with postprint thermal annealing, ACS Appl. Mater. Interfaces 9 (14) (2017) 12719–12727, https://doi.org/10.1021/acsami.7b00092.
[34] H.-H.- Huang, K.K.H. De Silva, G.R.A. Kumara, M. Yoshimura, Structural evolution of hydrothermally derived reduced graphene oxide, Sci. Rep. 8 (2018) 6849, https://doi.org/10.1038/s41598-018-25194-1.
[35] H. Ramamoorthy, K. Buapan, T. Chiawchan, K. Thamkrongart, R. Somphonsane, Exploration of the temperature-dependent correlations present in the structural, morphological and electrical properties of thermally reduced free-standing graphene oxide papers, J. Mater. Sci. 56 (2021) 15134–15150, https://doi.org/10.1007/s10853-021-06262-w.
[36] L. David, G. Singh, Reduced graphene oxide paper electrode: opposing effect of thermal annealing on Li and Na cyclability, J. Phys. Chem. C 118 (2014) 28401–28408, https://doi.org/10.1021/jp5080847.
[37] S.Y. Huang, B. Zhao, K. Zhang, M.M.F. Yuen, J.B. Xu, X.Z. Fu, R. Sun, C.P. Wong, Enhanced reduction of graphene oxide on recyclable Cu foils to fabricate graphene films with superior thermal conductivity, Sci. Rep. 5 (2015) 14260, https://doi.org/10.1038/srep14260.
[38] C. Vallés, J.D. Núñez, A.M. Benito, W.K. Maser, Flexible conductive graphene paper obtained by direct and gentle annealing of graphene oxide paper, Carbon 50 (3) (2012) 835–844, https://doi.org/10.1016/j.carbon.2011.09.042.
[39] Variable densification of reduced graphene oxide foam into multifunctional high-performance graphene paper, J. Mater. Chem. C 6 (2018) 12321–12328.
[40] F. Xu, R. Chen, Z. Lin, X. Sun, S. Wang, W. Yin, Q. Peng, Y. Li, X. He, Variable densification of reduced graphene oxide foam into multifunctional high-performance graphene paper, J. Mater. Chem. C 6 (2018) 12321–12328, https://doi.org/10.1039/C8TC04008G.
[41] C. Valentini, V. Montes-García, P.A. Livio, T. Chudziak, J. Raya, A. Ciesielski, P. Samorì, Tuning the electrical properties of graphene oxide through low temperature thermal annealing, Nanoscale 15 (2023) 5743–5755, https://doi.org/10.1039/D2NR06091D.
[42] A. Cernat, M. Tertis, R. Sandulescu, F. Bedioui, A. Cristea, C. Cristea, Electrochemical sensors based on carbon nanomaterials for acetaminophen detection: a review, Anal. Chim. Acta 886 (2015) 16–28, https://doi.org/10.1016/j.aca.2015.05.044.
[43] A. Lesch, S. Maye, M. Jović, F. Gumy, P. Tacchini, H.H. Girault, Analytical sensing platforms with inkjet printed electrodes, in: Biotech, Biomaterials and Biomedical TechConnect Briefs, Chapter 4, Sensors, Diagnostics & Imaging, 2016, ISBN 978-0-9975-1172-7, pp. 121–124. Washington, DC.
[44] G. Moro, A. Silvestri, A. Ulrici, F. Conzuelo, C. Zanardi, How to optimize the analytical performance of differential pulse voltammetry: one variable at time versus design of experiments, J. Solid State Electrochem. 28 (2024) 1403–1415, https://doi.org/10.1007/s10008-023-05753-x.
[45] B.A. Mei, O. Munteshari, J. Lau, B. Dunn, L. Pilon, Physical interpretations of Nyquist plots for EDLC electrodes and devices, J. Phys. Chem. C 122 (1) (2018) 194–206, https://doi.org/10.1021/acs.jpcc.7b10582.
[46] A. Ch Lazanas, M.I. Prodromidis, Electrochemical impedance spectroscopy – a tutorial, ACS Meas. Sci. Au 3 (2023) 162–193, https://doi.org/10.1021/acsmeasuresciau.2c00070.
[47] J.M. Savéant, Electrochemical approach to proton-coupled electron transfer: recent advances, Energy Environ. Sci. 5 (7) (2012) 7718–7731, https://doi.org/10.1039/C2EE03241D.
[48] S. Sundar, G. Venkatachalam, S.J. Kwon, Biosynthesis of copper oxide (Cuo) nanowires and their use for the electrochemical sensing of dopamine, Nanomaterials 8 (10) (2018) 823, https://doi.org/10.3390/nano8100823.
[49] S.P. Nayak, S.S. Ramamurthy, J.K. Kiran Kumar, Green synthesis of silver nanoparticles decorated reduced graphene oxide nanocomposite as an electrocatalytic platform for the simultaneous detection of dopamine and uric acid, Mater. Chem. Phys. 252 (2020) 123302, https://doi.org/10.1016/j.matchemphys.2020.123302.
[50] S. Baluta, F. Meloni, K. Halicka, A. Szyszka, A. Zucca, M.I. Pilo, J. Cabaj, Differential pulse voltammetry and chronoamperometry as analytical tools for epinephrine detection using a tyrosinase-based electrochemical biosensor, RSC Adv. 12 (39) (2022) 25342–25353, https://doi.org/10.1039/D2RA04045J.
[51] J. Gu, L. Fan, J. Bai, Z. Jin, T. Wei, Enhanced electrochemical detection of acetaminophen using CoNi-LDH-based sensor with ultra-wide linear range and superior performance, Anal. Bioanal. Chem. 417 (2025) 3741–3752, https://doi.org/10.1007/s00216-025-05901-4.
[52] E. Bayram, E. Akyilmaz, Development of a new microbial biosensor based on conductive polymer/multiwalled carbon nanotube and its application to paracetamol determination, Sens. Actuators, B 233 (2016) 409–418, https://doi.org/10.1016/j.snb.2016.04.029.
[53] D.E. Oh, C.S. Lee, T.H. Kim, Simultaneous and individual determination of seven biochemical species using a glassy carbon electrode modified with a nanocomposite of Pt nanoparticle and graphene by a one-step electrochemical process, Talanta 247 (2022) 123590, https://doi.org/10.1016/j.talanta.2022.123590.
[54] E.C. Martins, E.R. Santana, L.G. Baumgarten, J.P. Winiarski, J. de Bona, L.H. da Silveira Lacerda, G.A. Micke, G.M. de Oliveira Barra, I.C. Vieira, A. Spinelli, Disposable 3D-printed electrochemical sensor for in loco simultaneous monitoring of emerging pharmaceutical pollutants in aquatic ecosystems, J. Environ. Chem. Eng. 13 (2025) 119230, https://doi.org/10.1016/j.jece.2025.119230.
[55] E. Elanthamilan, S.F. Wang, Integration of NiCoFe layered double hydroxide@ graphitic carbon nitride composite: an electrochemical sensing platform for acetaminophen drug in water and urine samples, J. Environ. Chem. Eng. 13 (2025) 116929, https://doi.org/10.1016/j.jece.2025.116929.
[56] J. Rafi, T. Kokulnathan, T.J. Wang, M. Velmurugan, B. Neppolian, Evaluation of Fe-MOF/Graphene nanocompostites for non-enzymatic electrochemical sensing of acetaminophen, J. Mater. Chem. B (2026), https://doi.org/10.1039/d5tb02893k. Advance Article.
[57] X. Qi, Z. Wang, H. Yuan, H. Gao, X. Ren, H. Chen, H. Zhang, D. Chang, H. Pan, A novel electrochemical sensing based on cerium oxide/nitrogen-doped reduced graphene oxide for sensitive detection of acetaminophen, J. Electrochem. Soc. 171 (7) (2024) 077515, https://doi.org/10.1149/1945-7111/ad6296.
[58] L.P. Lin, P.S. Khiew, W.S. Chiu, M.T.T. Tan, A disposable electrochemical sensing platform for acetaminophen based on Graphene/ZrO_2 nanocomposite produced via a facile, green synthesis method, IEEE Sens. J. 18 (2018) 7907–7916, https://doi.org/10.1109/JSEN.2018.2864326.
[59] A.A. Lahcen, M. Sher, S. Ameer, G. Slaughter, Laser-induced graphene sensor for the electrochemical detection of acetaminophen, ChemistrySelect 10 (2025) e02914, https://doi.org/10.1002/slct.202502914.
[60] X. Cai, M. Li, R. Tao, X. Yang, J. Sun, C. Wei, Facile electrochemical determination of acetaminophen at micromolar levels utilizing conjugated bimetallic Co-Zn porphyrin polymer electrodes as sensing platforms, RSC Adv. 15 (2025) 21190–21198, https://doi.org/10.1039/D5RA00178A.
[61] L. Tang, Y. Huang, Y. Wang, H. Zhao, A flexible electrochemical sensor for simultaneous detection of acetaminophen and diclofenac sodium using a carbon nanotube-doped hydrogel, J. Electron. Mater. 54 (2025) 6218–6228, https://doi.org/10.1007/s11664-025-12056-6.
[62] P. Paíga, S. Figueiredo, M. Correia, M. André, R. Barbosa, S. Jorge, C. Deleure-Matos, Occurrence of 97 pharmaceuticals in wastewater and receiving waters: analytical validation and treatment influence, J. Xenobiotics 15 (2025) 78, https://doi.org/10.3390/jox15030078.